Supplementary information for

Cropland concentration powers sustainable intensification of agriculture in China

Shibin Liu[1,2,8]*, Long Ling[1,8], Fakun He[1,4,8], Jie Lei[1], Wenbin Huang[3], Jiamei Long[1], Jichong Han[5,6], Long Wan[1], Jiaguo Qi[7], Huaiyong Shao[1]*

1. College of Geography and Planning, Chengdu University of Technology, Chengdu 610059, Sichuan, China;
2. State Key Laboratory of Geohazard Provention and Geoenvironment Protection, College of Ecology and Environment, Chengdu University of Technology, Chengdu 610059, Sichuan, China;
3. College of Earth and Planetary Sciences, Chengdu University of Technology, Chengdu 610059, Sichuan, China;
4. Third Institute of Geoinformation Mapping, Ministry of Natural Resources, Chengdu 610100, Sichuan, China;
5. Key Laboratory of Environmental Change and Natural Disasters, School of National Safety and Emergency Management, Beijing Normal University, Beijing, China;
6. School of Systems science, Beijing Normal University, Beijing, China;
7. Center for Global Change and Earth Observations, Michigan State University, East Lansing, MI 48824, USA;
8. These authors contributed equally: Shibin Liu, Long Ling, Fakun He

***Corresponding authors:**
Shibin Liu (professor)
Affiliation: State Key Laboratory of Geohazard Provention and Geoenvironment Protection, College of Ecology and Environment, Chengdu University of Technology, Chengdu 610059, Sichuan, China;
E-mail: liushibin17@cdut.edu.cn

Huaiyong Shao (professor)
Affiliation: College of Geography and Planning, Chengdu University of Technology, Chengdu 610059, Sichuan, China;
E-mail: shaohuaiyong@cdut.edu.cn

Supplementary Notes

Supplementary Note 1: Details of data acquisition and processing

To address the issue of limited available data in certain regions, this study took the target year as the basis, and the year before and after the target year as the reference years. In this way, we selected a three-year image set for each period. For example, when using 2000 as the target year, all available images from 1999-2001 were utilized. For the target years of 2000, 2005, 2010, 2015, and 2020, this study collected 36,177, 43,810, 43,220, 58,232, and 53,365 Landsat remote sensing images, respectively, totaling 234,804 images (Supplementary Table 7). These image data were atmospherically corrected by the United States Geological Survey (USGS) through Landsat Ecosystem Disturbance Adaptive Processing System (LEDAPS) and the attached bands were used for masking to eliminate interference from clouds, shadows, water, snow, and ice[1].

Due to the spectral reflectance differences of OLI compared to previous sensors, we used conversion coefficients (Supplementary Table 8) to normalize OLI reflectance to TM and ETM+ reflectance. We repaired the stripe issue in ETM+ imagery using neighboring imagery. Firstly, we calculated the minimum mask of the image by applying a minimum value reduction operation to the mask layer, determining the minimum mask value for each pixel to identify missing data areas in the image. Secondly, by performing a neighborhood summation operation on the minimum mask layer, we assessed the mask coverage in the neighborhood of each pixel. The neighborhood summation results were then compared with a preset threshold to generate a Boolean layer, marking areas where the summation results were greater than or equal to the threshold as true, indicating regions potentially affected by stripes. Finally, by applying a logical and operation between the original mask and the generated Boolean layer, we updated the mask and eliminated the stripes. Sentinel-2 imagery, as well as terrain datasets derived from the Shuttle Radar Topography Mission (SRTM) Digital Elevation Model (DEM), were sourced from the Google Earth Engine (GEE) platform.

The agricultural statistical data used in this study, including the sown area of crops, the yield of major crops (i.e., rice, wheat, maize, legumes (soybeans, mung beans, and adzuki beans), and tuber crops (sweet potatoes and potatoes)), the application amount of agricultural fertilizers, and the total machinery power usage, were all sourced from the China Statistical Yearbook (http://www.stats.gov.cn/tjsj/ndsj/)[2]. Since the statistical data in each year's yearbook actually refer to the previous year, this study directly used the data from the yearbooks published in 2001, 2006, 2011, 2016, and 2021. Among them, the grain yield in the crop yield included cereals, legumes, and tubers. The yield calculation methods were as follows: cereals were calculated based on grain after threshing, legumes were calculated based on dry beans after removing the pods; tubers were calculated as 1 kg of grain for every 5 kg of fresh tubers; the application amount of agricultural fertilizers referred to the actual amount of fertilizer used in agricultural production in the target year, including nitrogen fertilizer, phosphate fertilizer, potassium fertilizer, and compound fertilizer, all calculated by pure weight. Nitrogen fertilizer, phosphate fertilizer, and potassium fertilizer are respectively converted according to the 100% content of nitrogen, phosphorus pentoxide, and potassium oxide, and compound fertilizers were converted according to their main components.

It is important to note that, compared to other developed countries in modern agriculture, China's mechanized agriculture started relatively late, but its development has been remarkably rapid[3]. To better evaluate the development of agricultural intensification, we focus on the impact brought by changes in total machinery power.

Moreover, since irrigation water use showed decreases from 2000 to 2020 for the whole country and most agricultural production zones (Supplementary Figure 4), we incorporated the irrigation water usage pattern into the evaluation matrix for analysis. The results show that it has a relatively smaller impact on the evaluation of sustainable agricultural intensification (Supplementary Table 5). Therefore, it was not included as a typical influencing factor in the evaluation matrix.

Supplementary Note 2: The establishment of the Random Forest classifier

To identify and label samples of cropland and non-cropland, we constructed a time-series viewer using GEE platform[4]. By calculating the Bare Soil Index (BSI) and Normalized Difference Vegetation Index (NDVI) for the years 2000, 2005, 2010, 2015, and 2020, and using Tasseled Cap transformation for Brightness, Greenness, and Wetness, in combination with high-resolution Google Earth imagery and corresponding cloud-free Landsat 5-8 and Sentinel 2 false color (RGB, NIR, SWIR1, Red) composite images, we developed a time-series viewer to identify stable cropland and non-cropland (Supplementary Figure 5). Based on this viewer, we manually selected pixels representing stable cropland and non-cropland through visual inspection as samples. These samples are land that maintained consistent land use types as either cropland or non-cropland from 2000 to 2020.

The BSI was used to capture soil signals when the cropland is tilled or harvested[5]. The BSI value ranges from -1 to 1, with higher values indicating a higher degree of soil exposure. The calculation formula is as follows:

$$\mathrm{BSI} = \frac{(\mathrm{SWIR2} + \mathrm{Red}) - (\mathrm{NIR} - \mathrm{Blue})}{(\mathrm{SWIR2} + \mathrm{Red}) + (\mathrm{NIR} - \mathrm{Blue})} \qquad (2\text{-}1)$$

where, SWIR2, Red, and Blue represent reflectance at short-wave infrared, red, and blue bands, respectively.

The Normalized Difference Vegetation Index (NDVI) reflects the vitality and nutritional status of vegetation. It is widely used to detect and identify vegetation changes. The NDVI value ranges from -1 to 1, with larger values indicating better vegetation growth[6]. The calculation formula is as follows:

$$\mathrm{NDVI} = \frac{\mathrm{NIR} - \mathrm{Red}}{\mathrm{NIR} + \mathrm{Red}} \qquad (2\text{-}2)$$

Where NIR represents the near-infrared band, and Red represents the red band.

The Tasseled Cap Transformation, also known as the K-T transform, projects the original image onto a brightness layer with physical significance according to a fixed transformation matrix. In the Tasseled Cap Transformation, we used the coefficients provided by Crist (1985) for the transformation[7] (Supplementary Table 9). Based on these methods, we conducted the labeling and selection of cropland and non-cropland samples.

We calculated a total of 44 variables to serve as input feature variables for the Random Forest classifier (Supplementary Table 10).

Supplementary Note 3: Method and results of accuracy assessment for cropland product dataset

To ensure a rational number of validating samples for both cropland and non-cropland, we randomly selected 20% of the samples from 2270 cropland and 3431 non-cropland samples, respectively. This resulted in 452 cropland and 689 non-cropland validating samples. These validating samples were imported into ArcGIS for accuracy assessment of the classification results. The sample accuracy measures include: Producer's Accuracy (PA) or omission error, User's Accuracy (UA) or commission error, Overall Accuracy (OA) for both cropland and non-cropland, and the Kappa coefficient. The calculation formulas for these accuracy evaluation metrics are as follows:

$$\mathrm{PA} = \frac{\mathrm{Nir}}{\mathrm{Nia}} \tag{3-1}$$

Where, N_{ir} represents the number of samples correctly classified as class i, and N_{ia} represents the actual number of reference samples in class i.

$$\mathrm{UA} = \frac{\mathrm{Nir}}{\mathrm{Nin}} \tag{3-2}$$

Where, N_{ir} represents the number of samples correctly classified as class i, and N_{in} represents the number of samples classified as class i.

$$\mathrm{OA} = \frac{\mathrm{Nr}}{\mathrm{Na}} \tag{3-3}$$

Where, N_r represents the number of samples correctly classified, and N_a represents the total number of samples.

$$\mathrm{Kappa} = \frac{\mathrm{OA} - P}{1 - P} \tag{3-4}$$

$$P = \frac{a_1 \times b_1 + a_2 \times b_2 + \cdots + a_i \times b_i}{n^2} \tag{3-5}$$

Where, OA represents the overall classification accuracy, a_i represents the actual number of samples in class i, b_i represents the number of samples in class i, and n represents the total number of samples.

The classification accuracy evaluation result of the cropland dataset can be found in Supplementary Table 1.

Supplementary Note 4: Division of nine agricultural production zones

The Northeast China Plain (NCP) is located in the northeast of China, including Heilongjiang Province, Jilin Province, and Liaoning Province, with a total area of about 8.7×10^5 km^2, primarily flat plains. The Northern arid and semiarid regions (NASR) is located in the north of China, including Inner Mongolia, Xinjiang, Gansu, and Ningxia, with a total area of about 3.3×10^6 km^2, encompassing hills, basins, and plains, with a wide range of altitudes. The Huang-Huai-Hai Plain (HHHP) is located in the northern part of eastern China, including Beijing, Tianjin, Hebei Province, Henan Province, and Shandong Province, with a total area of about 5.4×10^5 km^2, primarily flat plains and hills, most of which are below 50 meters in altitude. The Loess Plateau (LP) is located in the north-central part of China, including Shanxi and Shaanxi provinces, with a total area of about 3.6×10^5 km^2, mostly hilly, with altitudes ranging from 100 to 3500 meters. The Qinghai Tibet Plateau (QTP) is located in the southwestern plateau area of China, including the Tibet Autonomous Region and Qinghai Province, with a total area of about 1.8×10^6 km^2, primarily plateau, with an average altitude over 4000 meters. The Middle-Lower Yangtze Plain (MLYP) is located in the middle-east of China, including Anhui, Jiangsu, Jiangxi, Zhejiang, Hunan, Shanghai, Hubei, seven provinces and municipalities, with a total area of about 9.2×10^5 km^2, mainly plains and hills. The Sichuan Basin and surrounding regions (SCB) are located in the southwest of China, including Sichuan Province and Chongqing City, with a total area of about 5.7×10^5 km2, consisting of basins and hills, with pronounced terrain undulation. The Yunnan-Guizhou Plateau (YGP) is located in the southwest of China, including Yunnan, Guizhou, and Guangxi, with a total area of about 7.96×10^5 km^2. The Southern China (SC) is located in the south of China, including Guangdong, Fujian, Hainan, Taiwan, Macau, and Hong Kong. However, due to missing data, Hong Kong, Macau, and

Taiwan are not included in this study, with a total area of about 3.3×10^5 km^2, mostly hilly. The distribution of nine agricultural production zones can be found in Supplementary Figure 6.

Supplementary Note 5: Calculation method of landscape indexes

Landscape indexes can reflect the landscape pattern features of geographic entities, and are widely used to describe the landscape structure and spatial features of land cover. To profoundly reveal the characteristics of cropland changes in China, this study used three representative landscape indexes to describe the intensification degree of cropland, including Mean Patch Area (MPA), Patch Density (PD), and Aggregation Index (AI). They analyze the characteristics of cropland changes in China from three aspects: average cropland area, degree of fragmentation, and degree of aggregation. The calculation formulas are as follows:

$$\mathrm{MPA} = \frac{A}{\mathrm{NP}} \tag{5-1}$$

Where, A is the total area of cropland (ha), and NP is the number of cropland patches. This index reflects the average patch size and the degree of fragmentation of the cropland. The smaller the value, the greater the degree of cropland fragmentation.

$$\mathrm{PD} = \frac{\mathrm{NP}}{A} \tag{5-2}$$

Where, NP is the number of cropland, and A is the area of cropland (ha). PD represents the number of croplands per 100 ha. It is often used to describe the degree of spatial heterogeneity of the landscape and the degree of fragmentation of the landscape patches. The smaller the PD value, the smaller the degree of spatial heterogeneity of the cropland, and the higher the degree of concentration of the cropland.

$$\mathrm{AI} = \left[\sum_{i=1}^{m} \left(\frac{g_{i(i+1)}}{\max \rightarrow g_{i(i+1)}}\right) P_i\right] \times 100 \tag{5-3}$$

Where, $g_{i(i+1)}$ represents the adjacency between cropland patches i and i+1, and max→$g_{i(i+1)}$ is the maximum adjacency value between landscape type patches i and i+1. AI, Aggregation Index, reflects the degree of connectivity among the same type of landscape patches. When the fragmentation of a certain land type patch is most concentrated, the AI value approaches 0; when the aggregation degree of a certain land type patch is strongest, the AI value approaches 100.

In summary, the larger the MPA and AI values, and the smaller the PD value, the higher the concentration and contiguity of cropland, indicating greater spatial intensification and lower fragmentation. In this study, we used ArcGIS and Fragstats4.2 software to firstly disaggregate the 5-phase cropland data to obtain provincial cropland data, and then calculate the 5-phase landscape pattern index of cropland for each province using Fragstats 4.2 software. Other spatial analyzes in this study were performed in ArcGIS 10.6 software.

The calculation method for the rate of change in landscape indexes is as follows:

$$\mathrm{CM_{MPA}} = \frac{\mathrm{MPA}_{i+1} - \mathrm{MPA}i}{\mathrm{MPA}_i} \times 100\% \qquad (5\text{-}4)$$

$$\mathrm{CM_{PD}} = \frac{\mathrm{PD}_{i+1} - \mathrm{PD}i}{\mathrm{PD}_i} \times 100\% \qquad (5\text{-}5)$$

$$\mathrm{CM_{AI}} = \frac{\mathrm{AI}_{i+1} - \mathrm{AI}i}{\mathrm{AI}_i} \times 100\% \qquad (5\text{-}6)$$

Where, $\mathrm{CM_{MPA}}$, $\mathrm{CM_{PD}}$, $\mathrm{CM_{AI}}$ represent the rate of change for MPA, PD, and AI respectively, while MPA_i, PD_i, AI_i stand for the *MPA*, *PD*, and AI for the *i*-th period.

Supplementary Note 6: Calculation of the rate of change in agricultural production indicators

The calculation method for the rate of change in agricultural production indicators is as follows:

$$CF = \left(\frac{F_{i+1}}{A_{i+1}} - \frac{F_i}{A_i}\right) \times 100\% \quad (6\text{-}1)$$

$$CM = \left(\frac{M_{i+1}}{A_{i+1}} - \frac{M_i}{A_i}\right) \times 100\% \quad (6\text{-}2)$$

$$CY = \left(\frac{Y_{i+1}}{A_{i+1}} - \frac{Y_i}{A_i}\right) \times 100\% \quad (6\text{-}3)$$

Where, CF, CM, CY represent the change values of agricultural fertilizer application per unit area (kg ha^{-1}), total agricultural machinery power usage (kW ha^{-1}), and crop yield (t ha^{-1}), respectively. MPA_i, PD_i, AI_i represent the agricultural fertilizer application, total agricultural machinery power usage, and total crop yield in the i-th period, respectively. A_i represents the crop sowing area in the i-th period (ha).

Supplementary Note 7： Cropland Simulation Framework and Future Scenario Analysis

To provide a forward-looking assessment of China's cropland system, we used the calibrated Markov–CA framework to simulate the 2040 baseline scenario at a 30 m resolution. This projection offers insights into the likely direction and magnitude of future structural adjustments in cropland patterns, revealing the potential persistence or reorganisation of landscape characteristics. Detailed modeling settings and supplementary results are documented below.

Data Sources and Preprocessing

To capture the fine-scale characteristics of cropland patterns, we developed a spatially explicit dynamic simulation framework at a 30 m resolution, integrating both driver-factor learning and patch-generation mechanisms widely used in land-use change modeling. Because all spatial datasets in this study are available at a consistent 30 m resolution, the modeling was implemented under a unified national grid system, which helps preserve the geometric properties and local heterogeneity of cropland patches. Compared with land-use simulations conducted at kilometer-scale resolutions, the 30 m resolution enables a more accurate representation of the detailed spatial variation in cropland distribution, although it substantially increases the computational demands of data processing and model execution.

To ensure spatial consistency across data sources, all raster datasets were standardized to the spatial reference system of the baseline cropland map, including resampling to a uniform 30 m resolution, clipping to a consistent spatial extent, and applying an identical projection. To avoid scale distortions introduced by low-resolution variables, only datasets matching the baseline 30 m resolution were used; no downscaling procedures or low-accuracy variables were incorporated into model training.

In constructing the driver-factor system for cropland change, we considered both natural terrain conditions and human activities, forming a multi-category driver-factor database. (Supplementary Table 11). The selection of drivers followed insights from previous studies while balancing data accuracy and spatial coverage[8,9]. Two major groups of factors were included: (1) natural environmental drivers—digital elevation model (DEM), slope, and distance to rivers; and (2) socio-economic drivers—distance to prefecture-level city centers, distance to major roads, and distance to railways. All distance-based drivers were derived by calculating Euclidean distance from the corresponding vector datasets, producing continuous rasters aligned with the 30 m grid to represent spatial accessibility and potential development pressure at the pixel level.

To eliminate differences in units and improve numerical stability during model training, we applied min–max normalization to all driver variables, mapping their values to the range [0, 1].

$$x' = \frac{x - \min(x)}{\max(x) - \min(x)} \qquad (7\text{-}1)$$

where x is the original variable value and x' is the normalized value.

Cropland Expansion Driver Extraction

In constructing the spatial probability of cropland expansion, we followed the land-expansion analysis framework proposed by Liang et al. (2021), which transforms the identification of land-use change into a binary classification task[10]. Specifically, by overlaying land-use datasets from two periods, pixels that transitioned from non-cropland to cropland were identified and defined as positive samples, representing the spatial characteristics of newly added cropland. Pixels within the same evolutionary range that did not convert to cropland but were involved in land-use dynamics were defined as negative samples, providing contrasting conditions for learning where cropland expansion does not occur.

During the driver-factor extraction stage, we employed a Random Forest classifier to characterize the nonlinear relationships between multiple spatial drivers and cropland expansion. Random Forests consist of multiple decision trees capable of handling high-dimensional variables, capturing interactions among drivers, and maintaining strong robustness to noise. For pixel i, let x denote its vector of driving factors, and let the forest contain M decision trees. The prediction of the n-th decision tree based on x is represented by $h_n(x)$, where $h_n(x) = 1$ indicates that the pixel is predicted to convert to cropland in the next period, and $h_n(x) = 0$ indicates no expansion. Based on the voting results of all decision trees, the probability that pixel i will convert to cropland at the next time step, $\mathrm{P}_{i,k}^{1}(x)$, can be expressed as:

$$\mathrm{P}_{i,k}^{1}(x) = \frac{\sum_{n=1}^{M} \mathrm{I}(h_n(x) = 1)}{M} \qquad (7\text{-}2)$$

where $\mathrm{I}(\cdot)$ is an indicator function that equals 1 when the n-th tree predicts expansion and 0 otherwise. This probability reflects the aggregated judgement of the Random Forest and represents the likelihood of cropland conversion under the given driving conditions, forming the foundational input for the subsequent cellular automata–based spatial simulation.

Future Cropland Dynamics under the Baseline Scenario

Under the baseline scenario, we followed the conventional quantity–space coupling framework widely used in land-use change modeling by integrating the Markov process with a cellular automata (CA) approach to simulate the future spatial pattern of cropland. The Markov process was used to project the quantity of each land-use category in future periods, providing a macro-level constraint on land-use demand. The CA module then allocated these quantities spatially at the pixel level based on driving factors, neighborhood structure and spatial competition, thereby coupling macro-scale land-use demand with local spatial processes.

(1) Macro-level Demand Projection Using the Markov Process

The Markov process analyzes land-use data from two time periods to construct a transition probability matrix that describes the likelihood of conversion between land-use categories, thereby enabling the projection of future land-use quantities. Its basic form is expressed as:

$$A_{t+1} = A_t \mathrm{P} \tag{7-3}$$

Where A_t is the vector of land-use areas at time t.

$$A_t = \left[A_{1,t}, A_{2,t}, \dots, A_{n,t}\right] \tag{7-4}$$

with each element representing the area of land-use types 1 to n. P denotes the land-use transition probability matrix, in which each element P_{ij} represents the probability of land-use type i converting to type j during a transition step. It is calculated as:

$$\mathrm{P}_{ij} = \frac{N_{ij}}{\sum_{j=1}^{n} N_{ij}} \tag{7-5}$$

where N_{ij} is the number of pixels that changed from type i to type j during the observation period, and n is the total number of land-use categories. Once the transition probability matrix is obtained, multi-step land-use quantity changes can be derived through matrix exponentiation:

$$A_{t+k} = A_t \mathrm{P}^k \tag{7-6}$$

where k is the number of projection steps.

The resulting quantity vector provides the macro-level land-use demand constraints for the subsequent spatial simulation.

(2) Spatial Conversion Probability Under Quantity Constraints

In the spatial simulation, the evolution of future land-use patterns must satisfy both macro-level quantity constraints and local spatial processes. Within the CA framework, we constructed a comprehensive conversion probability for land-use type k at pixel i and iteration step t, representing the likelihood that the pixel will convert under the combined influence of driving factors, neighborhood configuration and macro-level demand. The comprehensive conversion probability $OP_{i,k}^{t}$ is defined as:

$$\mathrm{OP}_{i,k}^{t} = \mathrm{P}_{i,k}^{1} \times \Omega_{i,k}^{t} \times \mathrm{D}_{k}^{t} \tag{7-7}$$

where $\mathrm{P}_{i,k}^{1}$ denotes the probability that pixel i converts to land-use type k; D_{k}^{t} is the dynamic demand coefficient that adjusts the simulated area of land-use type k toward the macro-level target; and $\Omega_{i,k}^{t}$ is the neighborhood effect, which describes the degree of local spatial clustering around pixel i.

The neighborhood effect reflects the spatial autocorrelation of land-use types, meaning that a pixel is more likely to convert to type k if neighbouring pixels already belong to k. For an $n \times n$ neighborhood window, the neighborhood effect is expressed as:

$$\Omega_{i,k}^{t} = \frac{\mathrm{con}(c_i^{t-1} = k)}{n^2 - 1} \cdot \mathrm{w}_k \tag{7-8}$$

where $\mathrm{con}(c_i^{t-1} = k)$ is the number of neighbouring pixels belonging to type k at iteration step $t-1$; $n^2 - 1$ is the number of pixels in the neighborhood excluding the center pixel; and w_k is the spatial weight that controls the aggregation level of type k.

The dynamic demand coefficient D_k^t is formulated as:

$$\mathrm{D}_{k}^{t} = 1 + \beta \frac{\mathrm{A}_k^* - \mathrm{A}_k^t}{\left|\mathrm{A}_k^* - \mathrm{A}_k^t\right| + \mathrm{A}_k^*} \tag{7-9}$$

where β is the demand feedback coefficient that regulates the convergence speed, A_k^t is the simulated area of type k at iteration step t, and A_k^* is the target area predicted by the Markov process.

(3) Patch Generation Mechanism

During the evolution of land-use patterns, relying solely on neighborhood effects may prevent certain land-use types from forming new patches in previously unoccupied areas, thereby reducing the ecological realism of the simulated spatial pattern. To address this issue, a patch generation mechanism was incorporated into the CA simulation to allow the spontaneous emergence of a limited number of new patches in areas lacking neighborhood support.

When land-use type k is completely absent from the neighborhood of pixel i (i.e., $\Omega_{i,k}^{t} = 0$), potential new patch formation is triggered through stochastic perturbation. The comprehensive conversion probability is defined as:

$$\mathrm{OP}_{i,k}^{t} = \begin{cases} \mathrm{P}_{i,k}^{1} \times (r \times \mu_k) \times \mathrm{D}_k^t, & \text{if } \Omega_{i,k}^{t} = 0 \text{ and } r < \mathrm{P}_{i,k}^{1} \\ \mathrm{P}_{i,k}^{1} \times \Omega_{i,k}^{t} \times \mathrm{D}_k^t, & \text{all others} \end{cases} \quad (7\text{-}10)$$

where $\mathrm{P}_{i,k}^{1}$ is the probability of conversion to type k derived from driving factors; $r \in (0,1)$ is a random value introducing stochasticity; μ_k controls the difficulty of generating new patches of type k; $\Omega_{i,k}^{t}$ is the neighborhood effect; D_k^t is the dynamic demand coefficient.

To prevent excessive generation of new patches, a gradually decreasing conversion threshold was applied, allowing strict control of stochastic expansion during early iterations while progressively permitting more conversions later to ensure convergence[11]. When no pixel changes state in a given iteration ($\mathrm{N}_{\mathrm{change}} = 0$), the threshold is reduced according to:

$$\text{If } \mathrm{N}_{\mathrm{change}} = 0, l = l + 1, \tau_t = \tau_{t-1}\delta = \tau_0\delta^l. \quad (7\text{-}11)$$

The conversion rule is then:

$$\begin{cases} \text{Change}, & \mathrm{OP}_i^t \geq \tau_t, \\ \text{No change}, & \mathrm{OP}_i^t < \tau_t. \end{cases} \qquad (7\text{-}12)$$

where N_{change} is the number of pixels that successfully change state during the iteration; l is the number of threshold decay steps; τ_t is the conversion threshold at iteration t, δ is the decay coefficient; τ_{t-1} is the threshold used in the previous iteration; and OP_i^t is the comprehensive conversion probability of pixel i at time t.

Parameter Sensitivity Analysis

To systematically evaluate the influence of key parameters in the spatial evolution rules on the simulation results, five representative provinces—Jiangsu, Anhui, Jilin, Ningxia and Guizhou—were selected as experimental regions. These provinces cover typical geomorphological settings including plains, hills, humid mountain areas, arid regions and plateau–hill landscapes, thereby providing a comprehensive basis for assessing the model's applicability under diverse natural environmental conditions.

Based on the nationally unified set of driving factors, combinations of three core parameters (λ, δ, μ) were designed, resulting in 27 parameter configurations. The tested ranges were λ= 0.5–0.7, δ= 0.92–0.96 and μ= 0.001–0.005. Using land-use change during 2010–2020 as the reference period, each parameter combination was applied to the five provinces to generate simulated land-use maps for 2020. The simulation outputs were compared with the observed land-use data to compute the Figure of Merit (FoM), Overall Accuracy (OA) and the Kappa coefficient, which together provided a quantitative assessment of the performance of each parameter combination. Among these metrics, the FoM was primarily used to evaluate the relative differences among parameter sets rather than the absolute accuracy of the model.

To obtain the most robust parameter configuration for nationwide simulation, a multi-criteria ranking strategy was adopted. The median FoM across the five provinces was used as the primary selection criterion: a larger median value indicates better applicability across multiple regions. If multiple parameter combinations shared the highest median, their mean FoM values were compared, with a larger mean indicating superior overall performance. In cases where the mean values remained tied, the variance was used as the final criterion, favoring combinations with lower variance to ensure stable cross-regional performance. Based on this procedure, the parameter set λ= 0.5, δ= 0.96, μ= 0.005 was selected as the optimal configuration for the national-scale simulation, exhibiting the highest median FoM (0.36595) across the five provinces and demonstrating strong stability and adaptability across different geomorphic zones (Supplementary Table 12).

Model Implementation and Accuracy Assessment

The model was developed and executed in a Python 3.9 environment. The spatial probability extraction module was implemented using NumPy and Scikit-learn, with a Random Forest classifier used to generate the cropland expansion probability surface. The spatial dynamic evolution module employed Rasterio for raster input/output operations and NumPy for neighborhood computation and threshold decay procedures. Joblib was used to parallelize provincial simulation tasks to improve computational efficiency and scalability for large-area modeling. The national simulation was performed using a "province-level independent execution followed by final mosaicking" strategy to avoid excessive memory usage and reduce the risk of local optima arising from overly large spatial extents.

Model accuracy was evaluated using Overall Accuracy (OA), the Kappa coefficient and the Figure of Merit (FoM). OA and Kappa quantify the agreement between simulated and observed land-use maps, while FoM measures the spatial match of change locations. The validation results (Supplementary Figure 10) show a FoM of

0.10. FoM is known to be strongly affected by spatial resolution, change intensity and validation protocols, and previous studies have reported FoM values for land-use change products typically ranging from 0.1 to 0.3[12]. Therefore, the obtained FoM of 0.10 represents a reasonable and acceptable level of change simulation accuracy under the current resolution and evaluation conditions.

Future Cropland Projection and Landscape Pattern Analysis

After completing the model accuracy assessment, the established simulation framework was used to predict the spatial distribution of cropland in China in 2040 under the baseline scenario (Supplementary Figure 11) and the corresponding change pattern from 2020 to 2040 (Supplementary Figure 12). The simulation output maintains the same 30-m resolution and spatial extent as the 2020 baseline dataset, ensuring full spatial comparability between periods. This prediction provides a high-resolution basis for characterizing future cropland dynamics and analyzing subsequent changes in landscape structure.

To analyse the changes in cropland spatial structure, we calculated three typical landscape indicators—MPA, PD and AI—based on the cropland data for 2020 and 2040. All three indicators were independently computed at the provincial scale using the landscapemetrics package in R, representing cropland patch size, fragmentation level and spatial aggregation, respectively (Supplementary Table 13).

Using the Freedman–Diaconis rule, we determined the bin width H and applied ±H as the threshold to classify the rate of change in each index into three change patterns: increase (I), stable (S), and decrease (D) (Supplementary Table 14). Subsequently, at the provincial level, the three landscape indexes—MPA, PD and AI—were classified accordingly to derive the corresponding change pattern type for each province, and these were then summarized to produce the provincial-scale classification of landscape structural change (Supplementary Table 15).

Between 2020 and 2040, the spatial patterns of change in the three cropland landscape indexes indicate that the landscape structure in most provinces remains generally stable (Supplementary Figure 13). The proportions of the stable (S) category for MPA, PD and AI are 61.29%, 48.39% and 51.61%, respectively, suggesting that patch size, fragmentation and aggregation levels exhibit limited variation in the majority of provinces. Meanwhile, 32.26% of provinces show an increasing trend in MPA, 38.71% show a decreasing trend in PD, and 29.03% show an increasing trend in AI, indicating that some regions are experiencing larger patch sizes, reduced fragmentation or enhanced aggregation. Overall, China's future cropland landscape is dominated by structural stability, although moderate adjustments still occur.

The combined classification of the three indexes further reveals the spatial trajectories of cropland landscape evolution. The "structurally stable" type (S–S–S) is mainly distributed across most provinces in East, Central and North China, where all three indexes remain stable with minimal structural change. The "aggregation-enhancing" type (I–D–I) is concentrated in the southeastern coastal region and parts of central China, characterized by increasing patch size, decreasing patch numbers and enhanced aggregation, suggesting a shift toward more contiguous and intensified cropland configurations. The "intensified fragmentation" type (D–I–D) appears only in Heilongjiang and Liaoning, where decreasing patch size, increasing patch numbers and declining aggregation indicate a worsening level of fragmentation.

Overall, cropland landscape evolution in China is characterized by a predominance of stability, emerging intensification trends in the eastern and parts of the central region, and locally aggravated fragmentation in the northeast. These spatial differences reflect heterogeneous trajectories of cropland use and landscape structural adjustment across regions, offering important insights for future region-specific cropland protection and landscape optimization strategies.

Supplementary Note 8: Input Uncertainty Propagation Analysis

To assess the impact and propagation effects of input data discrepancies on the calculation of landscape pattern metrics, we conducted an uncertainty propagation analysis. This analysis aimed to quantify the response of landscape indexes results to variations in input data, thereby evaluating the robustness and reliability of the outcomes.

Input Discrepancy Assessment

The analysis was conducted using data from 31 provincial-level administrative units across China (excluding Hong Kong, Macao, and Taiwan) at five time points: 2000, 2005, 2010, 2015, and 2020. Based on the comparison between the cropland dataset generated in this study (Mine dataset) and the CLCD dataset[13], we calculated the relative difference in cropland area for each province to characterize the inconsistency between input datasets. The input difference (X) was defined as:

$$X = \frac{|A_{\text{Mine}} - A_{\text{CLCD}}|}{A_{\text{Mine}}} \times 100\% \qquad (8\text{-}1)$$

where A_{Mine} and A_{CLCD} represent the cropland areas (km²) from the Mine and CLCD datasets, respectively, and X denotes the relative deviation (%) between the two input datasets.

Result Difference Quantification

Landscape pattern metrics including Mean Patch Area (MPA), Patch Density (PD), and Aggregation Index (AI) were calculated based on the two input datasets. The result difference was quantified as follows:

$$Y_i = \frac{|I_{\text{i,Mine}} - I_{\text{i,CLCD}}|}{I_{\text{i,Mine}}} \times 100\% \qquad (8\text{-}2)$$

where I_{i} represents the value of the i-th landscape indexes. Y_i denotes the percentage difference in results. In total, 155 paired samples were obtained for each landscape indexes.

Model Fitting

To characterize the propagation relationship between input difference (*X*) and result difference (*Y*), we employed a logarithmic regression model. Given that both input and result differences are strictly positive percentage variables and exhibit right-skewed distributions, logarithmic transformation was applied to reduce the influence of extreme values and linearize their proportional relationship. The model is expressed as:

$$\log(Y_{\mathrm{i}} + \varepsilon) = \alpha_{\mathrm{i}} + \beta_{\mathrm{i}} X + \epsilon \qquad (8\text{-}3)$$

Exponentiating both sides yields:

$$Y_{\mathrm{i}} = e^{\alpha_i} \cdot e^{\beta_{\mathrm{i}} x} \qquad (8\text{-}4)$$

where Y_i denotes the result difference (%) of the i-th landscape indexes (MPA, PD, or AI), X represents the input cropland area difference (%), ε is a small constant to avoid taking the logarithm of zero, ϵ is the random error term, e denotes Euler's number, the base of the natural logarithm, and β_{i} is the sensitivity coefficient.

Output Relative Change Rate

To facilitate the interpretation of the physical meaning of the sensitivity coefficient β_{i}, we further define the relative change rate of the output metric R_i as:

$$R_{\mathrm{i}} = e^{\beta_{\mathrm{i}} \Delta X} - 1 \qquad (8\text{-}5)$$

where R_{i} represents the relative change rate of the i-th landscape indexes, β_{i} is the sensitivity coefficient, and ΔX denotes the increase in input difference (%). This equation quantifies the proportional change in the output metric when the input difference increases by ΔX percentage points.

Regression Results and Interpretation

The regression analysis revealed the extent of error propagation from input data discrepancies to landscape indexes outcomes. Interpreting the β coefficient as a measure of propagation magnitude, a 1% increase in input cropland area difference results in an average change of approximately 2.56% in the aggregation index (AI), indicating a relatively stronger transmission effect. In contrast, the corresponding changes in mean patch area (MPA) and patch density (PD) are approximately 1.12% and 1.42%, respectively. These results suggest that although input data discrepancies do propagate to metric outcomes, the overall magnitude of such effects is modest and does not compromise the robustness of the main conclusions (Supplementary Figure 9).

Supplementary Figures

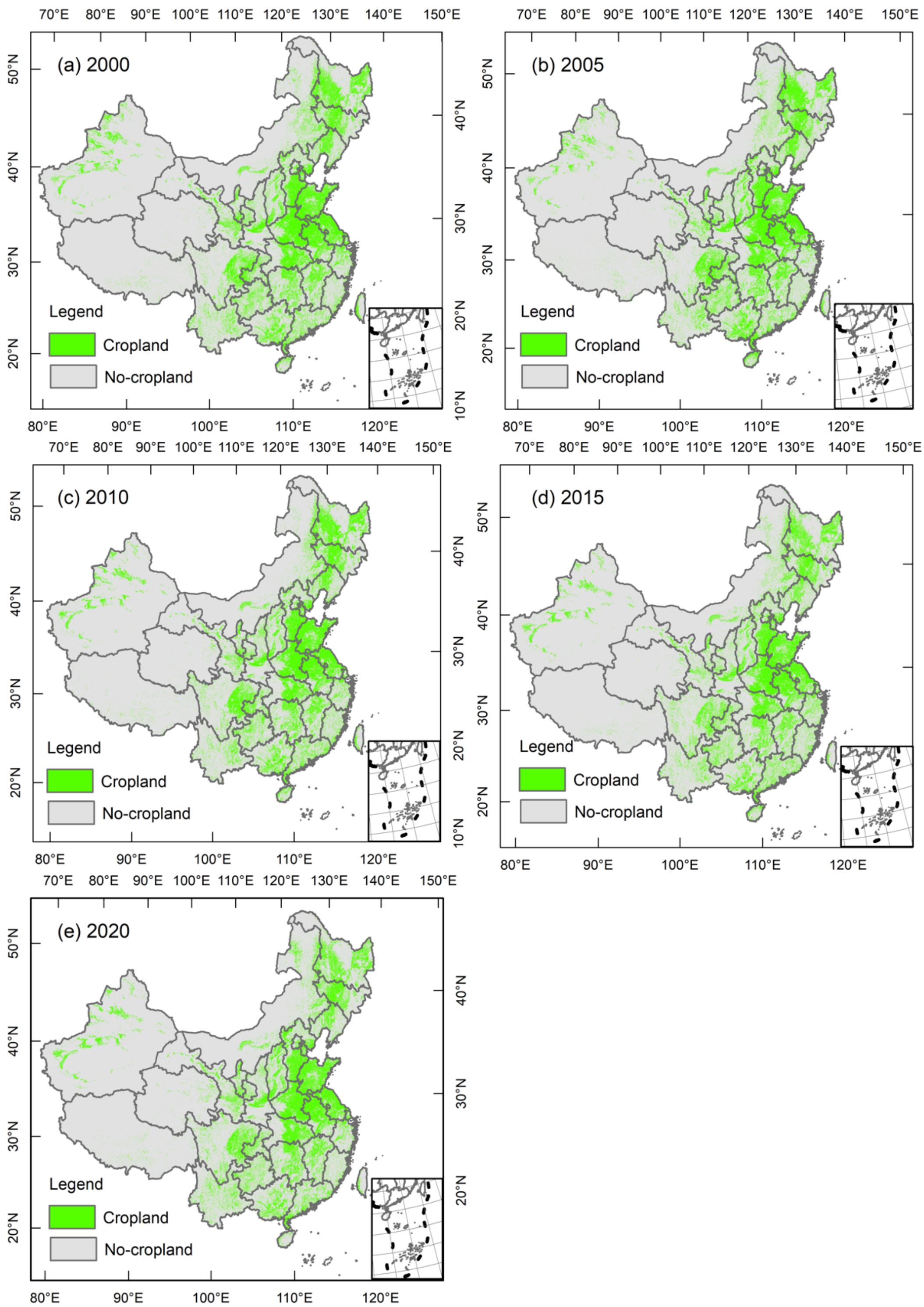

Supplementary Figure 1 | Cropland distribution from 2000 to 2020. Based on the established Random Forest inversion model, cropland dataset for 5-phase (i.e., (a) 2000, (b) 2005, (c) 2010, (d) 2015, (e) 2020) was obtained through pixel-by-pixel calculation.

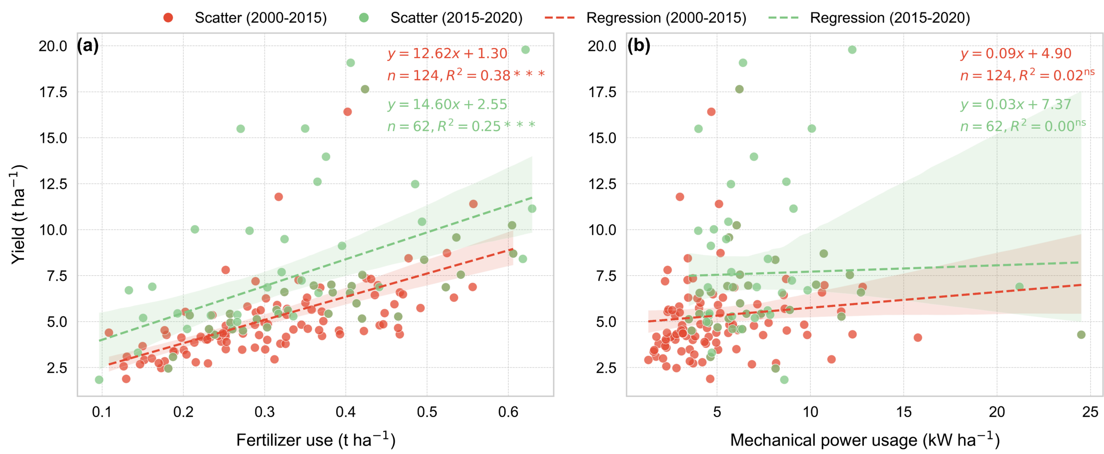

Supplementary Figure 2 | Correlations between yield and agricultural production indicators during the contraction (2000–2015) and recovery (2015–2020) periods. The scatter plots illustrate the linear regression analysis of yield (t ha^{-1}) in response to (a) fertilizer use (t ha^{-1}) and (b) machinery power usage (kW ha^{-1}). Red data points and dashed lines represent the contraction period (2000–2015), while green data points and dashed lines correspond to the recovery period (2015–2020). Statistical annotations include the linear regression equation, sample size (n), coefficient of determination (R^2), and significance levels. Significance is denoted as follows: *** $p < 0.001$, ** $p < 0.01$, * $p < 0.05$, and ns indicates not significant ($p \geq 0.05$). Shaded bands around the regression lines represent the 95% confidence intervals.

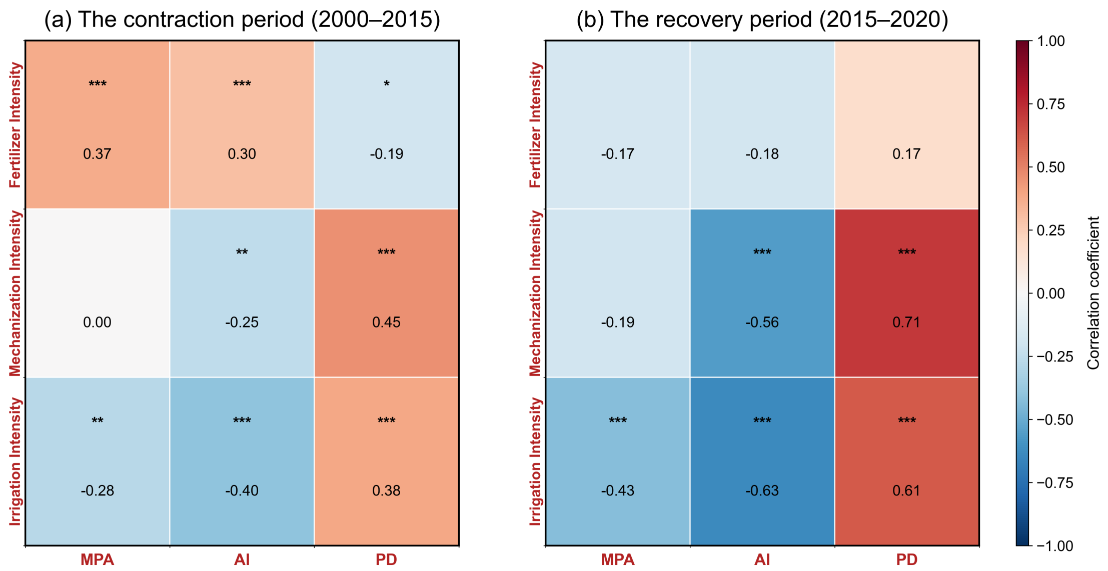

Supplementary Figure 3 | Correlation between cropland landscape configuration and agricultural input intensity across periods. Pearson correlation heatmaps between landscape pattern indexes (MPA, AI, PD) and agricultural input intensity indicators (fertilizer, mechanization, and irrigation intensity). (a) Contraction period (2000–2015); (b) Recovery period (2015–2020). The correlation analysis is based on provincial-level data across 31 regions in mainland China. Asterisks indicate significance levels (*p < 0.05, **p < 0.01, ***p < 0.001).

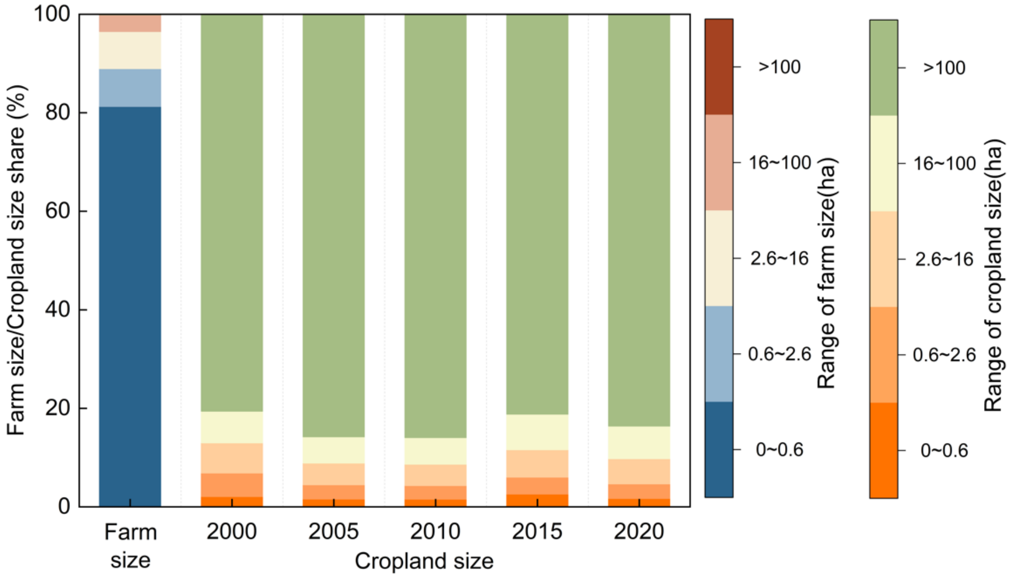

Supplementary Figure 4 | Proportion of farm size and cropland size in each range. The data of farm size were derived from Lesiv et al.35. "Farm size" is the area of cropland that has already achieved scale operation "cropland size" refers to the area of contiguous cropland patches.

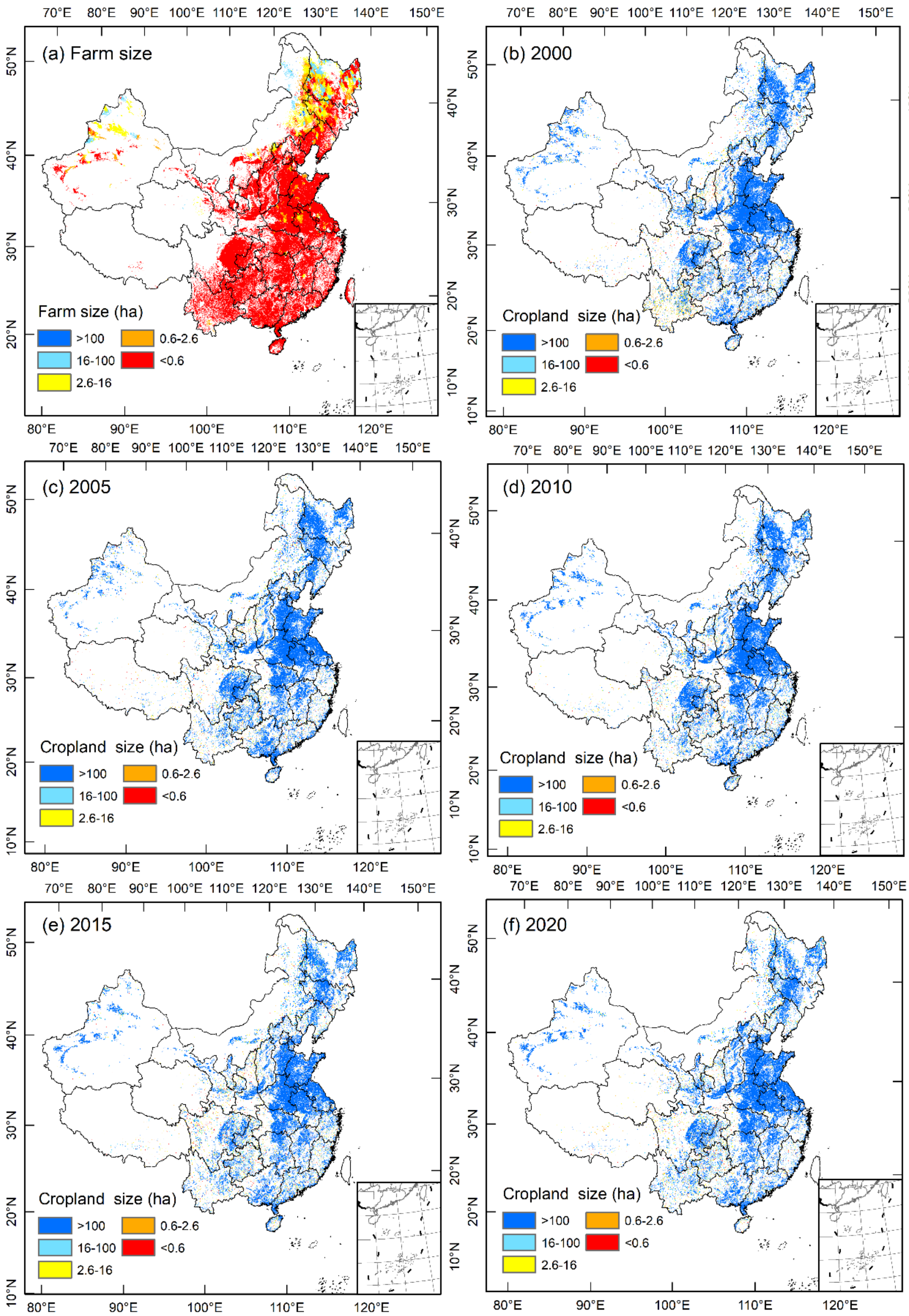

Supplementary Figure 5 | Map of farm size (a) and cropland size (b-f) in China. Farm size data was extracted from Lesiv et al.[14]. This paper categorized farm sizes into 5 categories: <0.6 ha, 0.6~2.6 ha, 2.6~16 ha, 16~100 ha and >100 ha.

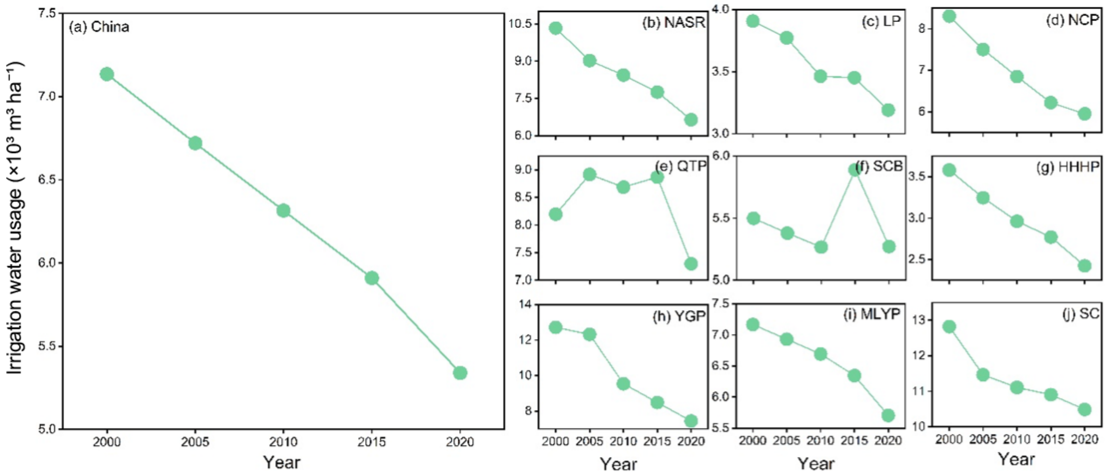

Supplementary Figure 6 |Irrigation water usage in China (a) and nine major agricultural production zones (b-j) during 2000-2020. The national provincial data on agricultural irrigation water usage were sourced from the Water Resources Bulletins publicly available on the official website of the Ministry of Water Resources of the People's Republic of China (http://www.mwr.gov.cn), including the publications from the years 2000, 2005, 2010, 2015, and 2020. Irrigated area data were sourced from the National Bureau of Statistics of China (https://www.stats.gov.cn/sj/ndsj/). Irrigation water usage for the nine major agricultural production zones was calculated based on the provincial irrigation water usage and irrigated area.

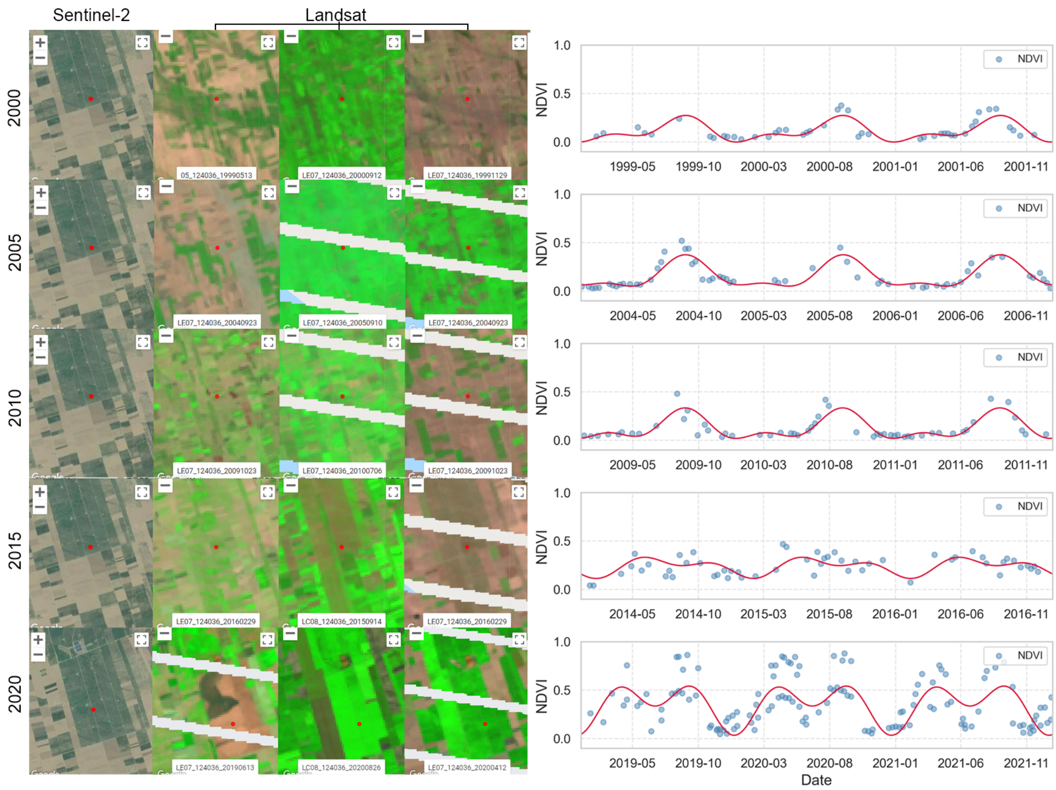

Supplementary Figure 7 | Sample selection time series viewing tool. This figure shows stable cropland at the location (113.15°E, 34.87°N) for each period. Each row presents Sentinel-2 imagery (10 m) and Landsat imagery (R, G, B: 7, 5, 4), accessed and visualized using Google Earth Engine, where the Landsat images are selected from within a one-year range centered around the target year. The selected sample is marked with a red dot. Below the imagery, time series of NDVI, BSI, Tasseled Cap Brightness, Greenness, and Wetness of the calibration sample are plotted. L4_7_SR stands for Landsat 4–7 surface reflectance, L8_SR indicates Landsat 8 surface reflectance, and S2_TOA refers to the top-of-atmosphere reflectance of Sentinel-2A and 2B. In this study, lands used for crop cultivation during the sampling period were treated as cropland samples.

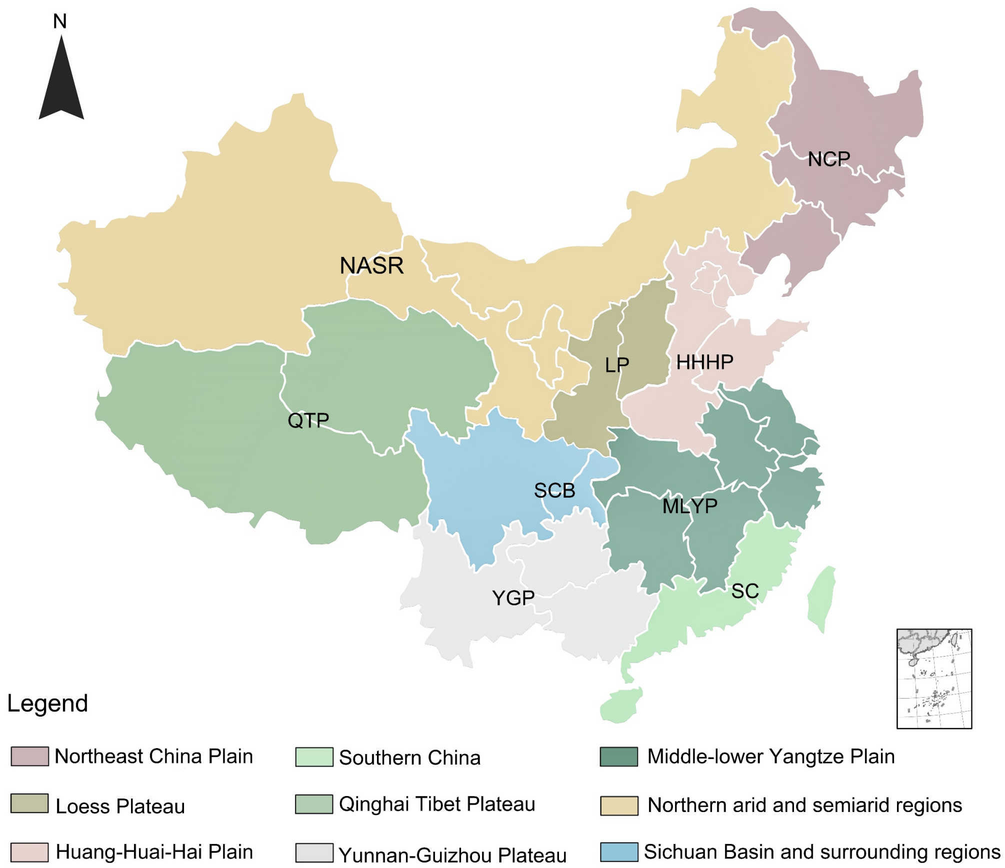

Supplementary Figure 8 | Distribution of nine agricultural production zones. These nine agricultural production zones are NCP (Northeast China Plain), NASR (Northern arid and semiarid regions), HHHP (Huang-Huai-Hai Plain), LP (Loess Plateau), QTP (Qinghai Tibet Plateau), MLYP (Middle-Lower Yangtze Plain), SCB (Sichuan Basin and surrounding regions), YGP (Yunnan-Guizhou Plateau) and SC (Southern China).

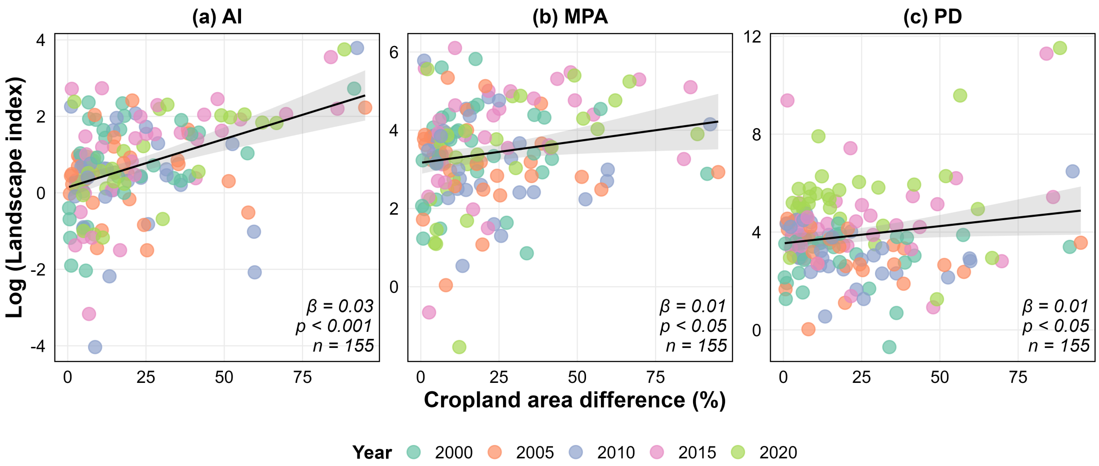

Supplementary Figure 9 | Relationships between provincial cropland area difference and three log-transformed landscape indexes from 2000 to 2020. (a) aggregation index (AI), (b) largest patch index (MPA), and (c) patch density (PD). Points show yearly observations. The black line indicates the linear regression fit, and the gray shading shows the 95% confidence interval. β, p, and n represent the regression slope, statistical significance, and sample size, respectively.

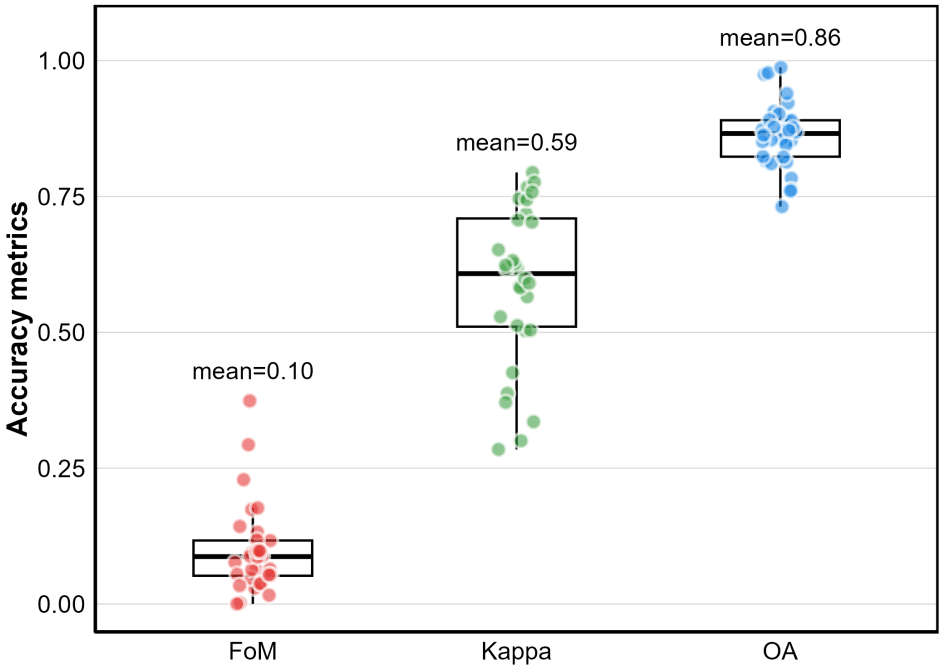

Supplementary Figure 10 | Accuracy metrics of the land-use simulation model. Box plots show the distribution of three accuracy indicators — the Figure of Merit (FoM), Kappa coefficient, and Overall Accuracy (OA) — across all provinces (n = 31). Each dot represents the model performance for one province. Boxes indicate the interquartile range (IQR; 25th–75th percentiles), center lines denote the median, and whiskers extend to 1.5 × IQR. The mean value for each metric is annotated above the corresponding box.

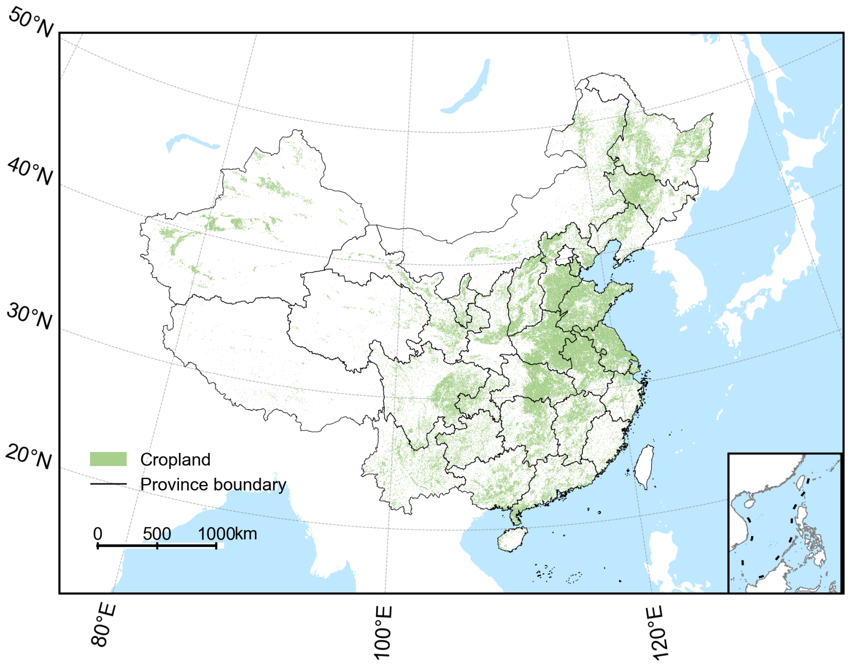

Supplementary Figure 11 | Spatial distribution of cropland in China in 2040.

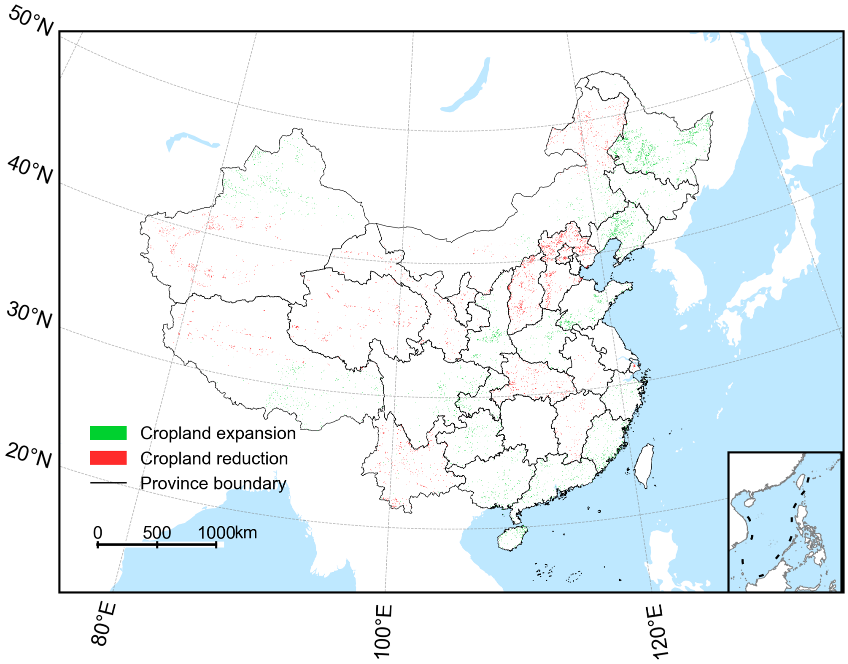

Supplementary Figure 12 | Spatial distribution of cropland change in China from 2020 to 2040.

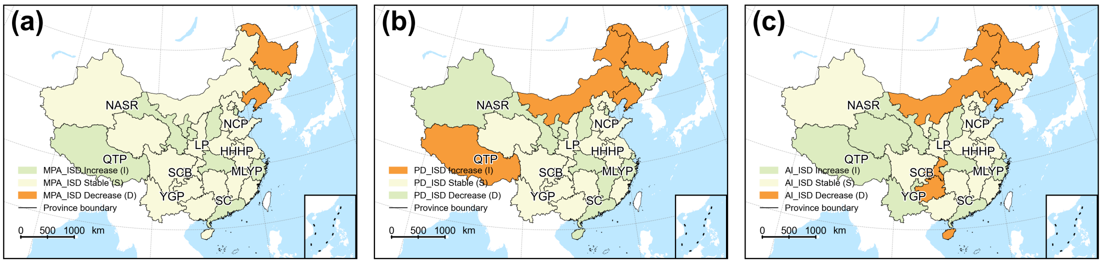

Supplementary Figure 13 | Spatial patterns of change patterns for 31 provincial-level administrative regions during 2020–2040. (a) shows the change patterns of mean patch area (MPA), (b) presents the change patterns of patch density (PD), and (c) illustrates the change patterns of the aggregation index (AI). 'I' represents an increase in the change pattern, 'S' represents a stable change pattern, and 'D' represents a decrease in the change pattern.

Supplementary Tables

Supplementary Table 1 | Classification accuracy evaluation results.

Year	Classification result	Validating sample		Total	User's accuracy
		Cropland	Non-cropland		
2000	Cropland	395	14	409	**96.58%**
	Non-cropland	57	675	732	**92.21%**
	Total	452	689	1141	
	Producer's accuracy	87.39%	97.97%		
	Overall accuracy	93.78%			
	Kappa	86.78%			
2005	Cropland	412	15	427	**96.49%**
	Non-cropland	40	674	714	**94.40%**
	Total	452	689	1141	
	Producer's accuracy	91.15%	97.82%		
	Overall accuracy	95.18%			
	Kappa	89.83%			
2010	Cropland	410	9	419	**97.85%**
	Non-cropland	42	680	722	**94.18%**
	Total	452	689	1141	
	Producer's accuracy	90.71%	98.69%		
	Overall accuracy	95.53%			
	Kappa	90.54%			
2015	Cropland	393	9	402	**97.76%**
	Non-cropland	59	680	739	**92.02%**
	Total	452	689	1141	
	Producer's accuracy	86.95%	98.69%		**94.04%**
	Overall accuracy	94.04%			
	Kappa	87.30			
2020	Cropland	411	14	425	**96.71%**
	Non-cropland	41	675	716	**94.27%**
	Total	452	689	1141	
	Producer's accuracy	90.93%	97.97%		
	Overall accuracy	95.18%			
	Kappa	89.82%			

Note: Among the 31 provincial-level administrative regions, the estimated cropland area is relatively high in Tibet, Qinghai, Xinjiang, Inner Mongolia, and Gansu because these regions have many pastures or grasslands, and the classifier used in the study may not be able to distinguish these two types of ground objects well. Furthermore, because the sample has used the same set for many years and the land surface type in the sample location remains consistent over the years, the actual accuracy estimate may be lower than the accuracy described in the text.

Supplementary Table 2 | Summary of the number of regions with different patterns of cropland and agricultural production indicators changes in each period.

Stage	Agricultural Production Indicators	Change Pattern	MPA			PD			AI		
			I	S	D	I	S	D	I	S	D
Contraction period	F	I	1	11	9	8	12	1	2	10	9
		S	0	5	4	4	5	0	0	6	3
		D	0	0	1	1	0	0	0	0	1
	M	I	1	16	13	12	17	1	2	16	12
		S	0	0	1	1	0	0	0	0	1
		D	0	0	0	0	0	0	0	0	0
	Y	I	1	12	11	10	13	1	2	12	10
		S	0	4	3	3	4	0	0	4	3
		D	0	0	0	0	0	0	0	0	0
	W	I	0	2	1	1	2	0	0	2	1
		S	0	7	1	1	7	0	0	3	5
		D	1	6	11	10	8	1	2	10	6
Recovery period	F	I	1	0	0	0	0	1	1	0	0
		S	8	2	0	1	0	9	5	5	0
		D	14	6	0	0	5	15	10	10	0
	M	I	3	1	0	1	0	3	2	2	0
		S	12	7	0	0	5	14	10	9	0
		D	8	0	0	0	0	8	4	4	0
	Y	I	10	4	0	1	2	11	6	8	0
		S	12	4	0	0	3	13	10	6	0
		D	1	0	0	0	0	1	0	1	0
	W	I	2	0	0	0	0	2	1	1	0
		S	9	3	0	1	1	9	6	5	0
		D	13	5	0	0	4	14	9	9	0

Supplementary Table 3 | Change patterns and sustainability intensification ratings for 31 provincial-level administrative regions after including irrigation water use in the agricultural production indicators.

Agricultural production zone	Provincial administrative region	2000-2015							Score	Grade	2015-2020							Score	Grade
		MPA	PD	AI	F	M	Y	W			MPA	PD	AI	F	M	Y	W		
NCP	Heilongjiang	D	I	D	I	I	I	D	-3	E	S	S	I	D	S	S	S	2	B
	Jilin	D	I	D	I	I	I	D	-3	E	I	D	S	D	S	S	S	3	B
	Liaoning	D	I	S	S	I	I	D	-1	D	S	S	S	D	S	I	D	3	B
NASR	Inner Mongolia	D	I	S	I	I	I	D	-2	D	S	S	S	D	S	I	D	3	B
	Xinjiang	I	D	I	I	I	I	D	3	B	I	D	S	S	S	S	D	3	B
	Gansu	D	I	D	S	I	I	S	-3	E	I	D	I	S	S	I	D	5	A
	Ningxia	S	S	I	I	I	I	D	1	C	I	D	I	S	D	S	D	5	A
HHHP	Beijing	D	I	D	I	I	I	D	-3	E	I	D	S	S	I	S	D	2	B
	Tianjin	D	I	D	I	S	I	D	-2	D	I	D	S	D	D	I	D	6	A+
	Hebei	S	S	S	I	I	I	D	0	C	I	D	S	D	D	S	S	4	A
	Shandong	D	I	S	S	I	I	D	-1	D	I	D	S	D	D	I	D	6	A+
	Henan	D	I	S	I	I	I	D	-2	D	I	D	S	D	D	D	D	4	A
LP	Shaanxi	S	S	S	I	I	I	S	-1	D	I	D	I	D	S	I	D	6	A+
	Shanxi	S	S	S	I	I	I	D	0	C	I	D	I	S	D	I	D	6	A+
QTP	Qinghai	S	S	S	S	I	S	I	-2	D	I	D	I	D	S	S	D	5	A
	Tibet	D	I	S	I	I	S	D	-3	E	I	D	I	D	D	S	D	6	A+
MLYP	Anhui	D	S	S	I	I	I	D	-1	D	I	D	S	D	S	S	S	3	B
	Jiangsu	D	I	D	S	I	I	I	-4	E	I	D	S	D	S	I	I	3	B
	Jiangxi	S	S	S	S	I	I	S	0	C	I	D	I	D	S	S	D	5	A
	Zhejiang	S	S	D	I	I	I	S	-2	D	I	D	I	D	D	S	S	5	A

Agricultural production zone	Provincial administrative region	2000-2015							Score	Grade	2015-2020							Score	Grade
		MPA	**PD**	**AI**	**F**	**M**	**Y**	**W**			**MPA**	**PD**	**AI**	**F**	**M**	**Y**	**W**		
MLYP	Hunan	S	S	S	S	I	S	D	0	C	I	D	I	S	I	I	D	4	A
	Shanghai	D	I	D	D	I	S	D	-2	D	I	D	I	S	S	S	S	3	B
	Hubei	S	S	D	I	I	I	S	-2	D	I	D	I	D	S	S	I	3	B
SCB	Sichuan	S	S	S	S	I	S	I	-2	D	S	D	I	D	S	S	S	3	B
	Chongqing	D	I	D	I	I	S	S	-5	F	S	D	S	S	S	I	D	3	B
YGP	Yunnan	S	S	D	I	I	I	D	-1	D	S	S	I	D	S	S	D	3	B
	Guizhou	S	S	D	S	I	S	S	-2	D	S	S	S	D	S	S	D	2	B
	Guangxi	S	S	S	I	I	I	D	0	C	I	D	S	S	S	I	S	3	B
SC	Guangdong	S	S	S	I	I	I	D	0	C	I	D	I	D	S	I	S	5	A
	Fujian	S	S	D	I	I	I	S	-2	D	I	D	I	I	I	I	S	2	B
	Hainan	S	S	S	I	I	I	S	-1	D	S	I	S	S	I	I	S	-1	D

Note: ‘I’ represents an increase in the change pattern, ‘S’ represents a stable change pattern, ‘D’ represents a decrease in the change pattern, ‘W’ represents irrigation water .

Supplementary Table 4 | Correlation between cropland landscape configuration and agricultural input intensity.

Period	Landscape index	Input intensity	N	Model	R^2	*p*-value
2000–2015	MPA	Fertilizer Intensity	124	OLS (univariate)	0.135	< 0.001
2015–2020		Fertilizer Intensity	62	OLS (univariate)	0.028	0.194
2000–2015		Mechanization Intensity	124	OLS (univariate)	0	0.957
2015–2020		Mechanization Intensity	62	OLS (univariate)	0.037	0.135
2000–2015		Irrigation Intensity	124	OLS (univariate)	0.079	0.002
2015–2020		Irrigation Intensity	62	OLS (univariate)	0.184	< 0.001
2000–2015	AI	Fertilizer Intensity	124	OLS (univariate)	0.092	< 0.001
2015–2020		Fertilizer Intensity	62	OLS (univariate)	0.034	0.153
2000–2015		Mechanization Intensity	124	OLS (univariate)	0.065	0.004
2015–2020		Mechanization Intensity	62	OLS (univariate)	0.312	< 0.001
2000–2015		Irrigation Intensity	124	OLS (univariate)	0.160	< 0.001
2015–2020		Irrigation Intensity	62	OLS (univariate)	0.401	< 0.001
2000–2015	PD	Fertilizer Intensity	124	OLS (univariate)	0.037	0.033
2015–2020		Fertilizer Intensity	62	OLS (univariate)	0.030	0.181
2000–2015		Mechanization Intensity	124	OLS (univariate)	0.207	< 0.001
2015–2020		Mechanization Intensity	62	OLS (univariate)	0.50	< 0.001
2000–2015		Irrigation Intensity	124	OLS (univariate)	0.148	< 0.001
2015–2020		Irrigation Intensity	62	OLS (univariate)	0.377	< 0.001

Notes: The table summarizes bivariate correlations between cropland landscape configuration and agricultural input intensity based on univariate ordinary least squares (OLS) regressions. Reported statistics include sample size (N), coefficients of determination (R^2), and p-values.

Supplementary Table 5 | Proportion of different cropland sizes in each agricultural production zone from 2000 to 2020.

Agricultural production zone	Phase	≤0.6 ha (%)	0.6-2.6 ha (%)	2.6-16 ha (%)	16-100 ha (%)	≥100 ha (%)
NCP	2000	0.77	1.38	2.98	4.54	90.33
	2005	0.66	1.16	2.4	3.86	91.92
	2010	0.66	1.28	2.74	4.64	90.69
	2015	1.93	2.35	4.9	8.85	81.97
	2020	1.64	2.21	4.82	8.25	83.08
NASR	2000	2.08	4.04	7.59	9.79	76.5
	2005	2.13	4.42	7.99	10.6	74.86
	2010	1.06	2.85	5.73	8.23	82.13
	2015	2.68	4.06	8.07	12.49	72.7
	2020	1.83	3.44	7.28	11.55	75.91
HHHP	2000	0.7	0.97	1.06	1.24	96.03
	2005	0.41	0.83	0.99	1.16	96.61
	2010	0.4	0.83	1	1.1	96.68
	2015	0.87	0.98	1.26	1.51	95.38
	2020	0.49	0.88	1.1	1.17	96.36
LP	2000	5.07	6.62	8.12	7.58	72.61
	2005	2.36	5.34	7.12	7.62	77.56
	2010	2.38	5.56	7.17	8.16	76.73
	2015	5.16	6.21	8.32	8.64	71.66
	2020	2.21	4.33	6.34	7.32	79.8
QTP	2000	14.89	15.05	18.57	19.06	32.43
	2005	10.73	13.25	19.67	20.93	35.42
	2010	7.03	12.02	20.85	23.53	36.58
	2015	16.51	14.37	18.87	20.45	29.79
	2020	7.29	13.15	18.13	18.48	42.95
MLYP	2000	1.56	2.19	2.67	2.7	90.89
	2005	0.91	1.98	2.49	2.74	91.88
	2010	0.96	1.91	2.65	3.04	91.45
	2015	1.83	2.25	3.17	3.63	89.13
	2020	0.81	1.65	2.58	2.85	92.1
SCB	2000	2.49	16.9	17.43	16.51	46.67
	2005	2.71	3.47	5.67	6.91	81.24
	2010	3.79	4.24	6.82	7.81	77.34

Agricultural production zone	**Phase**	**≤0.6 ha (%)**	**0.6-2.6 ha (%)**	**2.6-16 ha (%)**	**16-100 ha (%)**	**≥100 ha (%)**
SCB	2015	5.16	6.48	10.44	11.27	66.65
	2020	3.75	4.94	8.48	9.55	73.27
YGP	2000	4.76	9.03	10.81	7.66	67.74
	2005	2.31	5.71	7.69	8.43	75.86
	2010	3.08	6.5	8.6	9.25	72.56
	2015	3.82	6.6	9.48	10.42	69.67
	2020	3.3	6.28	10.48	12.03	67.91
SC	2000	4.02	4.93	8.32	9.9	72.82
	2005	3.58	4.7	6.99	8.08	76.66
	2010	3.73	4.48	7.77	10.14	73.89
	2015	3.94	5.21	9.27	11.85	69.72
	2020	2.03	4.35	7.34	8.73	77.55

Supplementary Table 6 | The number of Landsat images used in this study.

Year	Landsat 5	Landsat 7	Landsat 8	**Total**
1999	6043	1816		
2000	7056	6567		36177
2001	7176	7519		
2004	7449	8144		
2005	6305	7519		43810
2006	7047	7346		
2009	8620	7100		
2010	7383	6593		43220
2011	6342	7182		
2014		9208	10507	
2015		9020	10314	58232
2016		8757	10426	
2019		9040	10328	
2020		9034	10018	53365
2021		6928	8017	
Total	63421	111773	59610	234804

Supplementary Table 7 | Relationship between Landsat 8 OLI and Landsat 7 ETM+ reflectance.

Band	Conversion formula between OLI and ETM+ reflectance
Blue	ETM+=0.0219+0.8155OLI
Green	ETM+=0.0128+0.8911OLI
Red	ETM+=0.0128+0.9129OLI
Near infrared	ETM+=0.0438+0.7660OLI
Shortwave infrared 1	ETM+=0.0246+0.8286OLI
Shortwave infrared 2	ETM+=0.0075+0.8329OLI

Supplementary Table 8 | Landsat tasseled cap transformation coefficients matrix.

Index	Blue	Green	Red	NIR	SWIR1	SWIR2
Brightness	0.2043	0.4158	0.5524	0.5741	0.3124	0.2303
Greenness	-0.1603	-0.2819	-0.4934	0.794	-0.0002	-0.1446
Wetness	0.0315	0.2021	0.3102	0.1594	-0.6806	-0.6109

Supplementary Table 9 | Input feature variables of the Random Forest classifier.

Category	Variable name	Number of variables
NDVI/NDWI values	NDVI/NDWI (1st quarter)	6
	NDVI/NDWI (2nd quarter)	6
	NDVI/NDWI (3rd quarter)	6
	NDVI/NDWI (4th quarter)	6
NDVI Annual statistics	NDVI standard deviation, range, minimum	3
75% percentile	B1, B2, B3, B4, B5, B7, NDVI, NDWI	16
SRTM DEM	Slope factor	1
Total		44

Note: A total of 44 variables were computed as input variables for the classifier: NDVI and NDWI values for each quarter (24 variables; 1st quarter: days 1-90, 2nd quarter: days 91-180, 3rd quarter: days 181-270, 4th quarter: days 271-360); NDVI standard deviation, range, and minimum (3 variables); the 75% percentile of B1, B2, B3, B4, B5, B7, NDVI, and NDWI for the two years before and after each target year[15] (16 variables); and the slope factor calculated based on SRTM DEM (1 variable).

Supplementary Table 10 | Division of change patterns.

Stages	Change pattern	Landscape indexes and agricultural production indicators						
		AI	PD	MPA	F	M	Y	W
Contraction period	I	>1.44	>27.17	>18.41	>0.69	>0.57	>1.07	>0.12
	S	-1.44~1.44	-27.17~27.17	-18.41~18.41	-0.69~0.69	-0.57~0.57	-1.07~1.07	-0.12~0.12
	D	<-1.44	<-27.17	<-18.41	<-0.69	<-0.57	<-1.07	<-0.12
Recovery period	I	>3.18	>16.13	>58.02	>0.30	>0.97	>0.42	0.07
	S	-3.18~3.18	-16.13~16.13	-58.02~58.02	-0.30~0.30	-0.97~0.97	-0.42~0.42	-0.07~0.07
	D	<-3.18	<-16.13	<-58.02	<-0.30	<-0.97	<-0.42	<-0.07

Notes: The numbers in the table represent the threshold “H”. AI: Aggregation Index; PD: Patch Density; MPA: Mean Patch Area; F: Fertilizer use; M: Total machinery power usage; Y: Crop yield; W: Irrigation water; I: Increase; S: Stable; D: Decrease

Supplementary Table 11 | Input datasets for the 2040 cropland simulation.

Category	Data	Year	Resolution	Data resource
Natural environment	DEM (Digital Elevation Model)	2020	30 m	NASA SRTM1 v3.0
	Slope	2020	30 m	(https://lpdaac.usgs.gov/products/srtmgl1v003/)
Socio-economic factors	Distance torivers	2020	30 m	OpenStreetMap
	Distance to cities	2020	30 m	(https://www.openstreetmap.org/)
	Distance to mainroads	2020	30 m	
	Distance to railways	2020	30 m	
Land use data	Cropland and non-cropland map	2010,2020	30 m	Produced in this study based on remote sensing interpretation

Supplementary Table 12 | Summary of FoM statistics for the 27 parameter combinations (λ, δ, μ) across the five representative provinces.

λ	δ	μ	FoM (median)	FoM (mean)	FoM (variance)
0.5	0.96	0.005	0.365950706	0.366184386	0.000978135
0.5	0.96	0.003	0.365037223	0.365590437	0.00098228
0.5	0.92	0.003	0.364601233	0.366077786	0.000936174
0.5	0.92	0.005	0.364352387	0.366466332	0.000980118
0.5	0.94	0.005	0.364303188	0.366462993	0.001027998
0.5	0.92	0.001	0.364199188	0.365884999	0.000983797
0.5	0.94	0.001	0.364053797	0.366606312	0.001029956
0.5	0.96	0.001	0.363583585	0.366245624	0.001030562
0.5	0.94	0.003	0.363138299	0.3667156	0.000972018
0.6	0.92	0.003	0.365674704	0.365539231	0.000978896
0.6	0.96	0.003	0.365261416	0.366272063	0.000986535
0.6	0.96	0.001	0.36463788	0.365983083	0.000997214
0.6	0.94	0.003	0.364368316	0.36638105	0.000987051
0.6	0.92	0.001	0.363713427	0.366186574	0.000966423
0.6	0.94	0.001	0.363604703	0.366453206	0.000954513
0.6	0.92	0.005	0.363418107	0.366007779	0.000984248
0.6	0.94	0.005	0.363119751	0.366546704	0.000944405
0.6	0.96	0.005	0.363058244	0.366356501	0.000955257
0.7	0.96	0.003	0.365228481	0.366015894	0.000980037
0.7	0.94	0.001	0.365182889	0.365768114	0.000991507
0.7	0.92	0.005	0.365125186	0.365970382	0.001016164
0.7	0.94	0.005	0.365040352	0.365981059	0.001004144
0.7	0.92	0.003	0.364755171	0.365988231	0.000990967
0.7	0.94	0.003	0.364507181	0.365843685	0.000981438
0.7	0.92	0.001	0.36421249	0.366441628	0.000932203
0.7	0.96	0.005	0.363662527	0.366264252	0.000987476
0.7	0.96	0.001	0.363176336	0.36625195	0.000978286

Notes: FoM statistics (median, mean, variance) for the 27 parameter combinations (λ, δ, μ) across five provinces. Bold values indicate the highest FoM median, representing the optimal parameter set.

Supplementary Table 13 | Provincial landscape indexes in 2040.

province	MPA	PD	AI
Anhui	69.16883926	1.44573772	96.96177959
Beijing	16.50059736	6.060386651	92.21570716
Chongqing	7.56617653	13.21671515	85.5405915
Fujian	4.737688191	21.10734096	83.90536685
Gansu	32.45469	0.7572932	93.59637
Guangdong	12.20997274	8.190026477	90.19996932
Guangxi	10.58471825	9.4475826	90.72927783
Guizhou	4.134730843	24.18537114	79.95821417
Hainan	4.401365	3.198759	82.76022
Hebei	36.66127567	2.72767377	96.19483501
Heilongjiang	13.57867	1.398997	89.23713
Henan	82.25082499	1.215793276	97.36932817
Hubei	25.97365828	3.850054503	94.90635749
Hunan	15.8430457	6.311917664	91.39749621
Jiangsu	98.28854149	1.017412594	96.68840434
Jiangxi	19.56286929	5.111724589	91.73330675
Jilin	37.94444159	2.635432116	94.85890533
Liaoning	9.465577718	10.56459553	89.56480865
Neimenggu	10.65205385	0.640115591	59.23055983
Ningxia	16.67091081	5.998472499	92.16598869
Qinghai	5.179666717	19.30626148	88.20868179
Shaanxi	7.6078835	13.14426016	88.88046691
Shandong	67.0007146	1.492521395	96.51555161
Shanghai	57.84399395	1.728787955	94.28717328
Shanxi	20.697193	4.831573055	93.59622349
Sichuan	6.50418956	15.37470565	86.08352325
Tianjin	77.85407376	1.284454302	96.59422578
Xinjiang	41.8607001	0.10583875	95.3859791
Xizang	9.182418586	22.67072666	87.06430276
Yunnan	6.097463757	16.40026148	86.37547139
Zhejiang	11.98281069	8.345287479	89.95390072

Supplementary Table 14 | Division of change patterns (simulation).

Stages	Change pattern	Landscape indexes and agricultural production indicators		
		AI	PD	MPA
Simulation	I	>0.02	>0.28	>0.45
	S	-0.02~0.02	-0.28~0.28	-0.45~0.45
	D	<-0.02	<-0.28	<-0.45

Notes: The numbers in the table represent the threshold “H”. AI: Aggregation Index; PD: Patch Density; MPA: Mean Patch Area; F: Fertilizer use; M: Total machinery power usage; Y: Crop yield; W: Irrigation water; I: Increase; S: Stable; D: Decrease

Supplementary Table 15 | Change patterns for 31 provincial-level administrative regions in 2040.

Agricultural production zone	Provincial administrative region	Change patterns		
		MPA	PD	AI
NCP	Heilongjiang	D	I	D
	Jilin	I	D	S
	Liaoning	D	I	D
NASR	Inner Mongolia	S	I	D
	Xinjiang	S	D	S
	Gansu	I	D	I
	Ningxia	I	D	S
HHHP	Beijing	S	S	S
	Tianjin	I	D	S
	Hebei	S	S	S
	Shandong	S	S	S
	Henan	S	S	S
LP	Shaanxi	S	S	S
	Shanxi	I	D	I
QTP	Qinghai	S	S	I
	Tibet	I	I	I
MLYP	Anhui	S	S	S
	Jiangsu	S	S	S
	Jiangxi	S	D	S
	Zhejiang	S	S	S
	Hunan	S	S	S
	Shanghai	I	D	I
	Hubei	I	D	I
SCB	Sichuan	S	S	S
	Chongqing	S	S	D
YGP	Yunnan	S	S	I
	Guizhou	S	S	D
	Guangxi	S	S	S
SC	Guangdong	I	D	I
	Fujian	S	S	S

Note: 'I' represents an increase in the change pattern, 'S' represents a stable change pattern, and 'D' represents a decrease in the change pattern.

Supplementary References

1. Masek, J. G. *et al.* A Landsat surface reflectance dataset for North America, 1990-2000. *IEEE Geosci. Remote Sens. Lett.* **3**, 68-72 (2006).
2. National Bureau of Statistics of China. *China Statistical Yearbook 2016* https://www.stats.gov.cn/sj/ndsj/2016/indexeh.htm (2016).
3. Wang, X. B., Yamauchi, F. & Huang, J. K. Rising wages, mechanization, and the substitution between capital and labor: evidence from small scale farm system in China. *Agric. Econ.* **47**, 309-317 (2016).
4. Yin, H. *et al.* Monitoring cropland abandonment with Landsat time series. *Remote Sens. Environ.* **246**, 111873 (2020).
5. Rikimaru, A., Roy, P. & Miyatake, S. Tropical forest cover density mapping. *Trop. Ecol.* **43**, 39-47 (2002).
6. Kalisa, W. *et al.* Assessment of climate impact on vegetation dynamics over East Africa from 1982 to 2015. *Sci. Rep.* **9**, 16865 (2019).
7. Crist, E. P. A TM Tasseled Cap equivalent transformation for reflectance factor data. *Remote Sens. Environ.* **17**, 301-306 (1985).
8. Zhuang, H. M. *et al.* Simulation of urban land expansion in China at 30 m resolution through 2050 under shared socioeconomic pathways. *GISci. Remote Sens.* **59**, 1301-1320 (2022).
9. Li, X. C. *et al.* A cellular automata downscaling based 1 km global land use datasets (2010-2100). *Sci. Bull.* **61**, 1651-1661 (2016).
10. Liang, X. *et al.* Understanding the drivers of sustainable land expansion using a patch-generating land use simulation (PLUS) model: A case study in Wuhan, China. *Comput. Environ. Urban Syst.* **85**, 101569 (2021).
11. Liu, X. P. *et al.* A future land use simulation model (FLUS) for simulating multiple land use scenarios by coupling human and natural effects. *Landsc. Urban Plan.* **168**, 94-116 (2017).
12. Zhang, T. Y., Cheng, C. X. & Wu, X. D. Mapping the spatial heterogeneity of global land use and land cover from 2020 to 2100 at a 1 km resolution. *Sci. Data* **10**, 748 (2023).
13. Yang, J. & Huang, X. The 30 m annual land cover dataset and its dynamics in China from 1990 to 2019. *Earth Syst. Sci. Data* **13**, 3907-3925 (2021).
14. Lesiv, M. *et al.* Estimating the global distribution of field size using crowdsourcing. *Glob. Change Biol.* **25**, 174-186 (2019).
15. Teluguntla, P. *et al.* A 30-m landsat-derived cropland extent product of Australia and China using random forest machine learning algorithm on Google Earth Engine cloud computing platform. *ISPRS-J. Photogramm. Remote Sens.* **144**, 325-340 (2018).